Membrane wetting, molding and reticulation by protein condensates

Agustín Mangiarotti[1], Nannan Chen[1,2], Ziliang Zhao[1,3], Reinhard Lipowsky[1] and Rumiana Dimova[1]

[1] Max Planck Institute of Colloids and Interfaces, Science Park Golm, 14476 Potsdam, Germany

[2] Current address: Department of Nutrition and Food Hygiene, Guangzhou Medical University, Guangzhou 511436, China

[3] Current address: Leibniz Institute of Photonic Technology e.V., Albert-Einstein-Straße 9, 07745 Jena, Germany; and Institute of Applied Optics and Biophysics, Friedrich-Schiller-University Jena, Max-Wien Platz 1, 07743 Jena, Germany

Address correspondence to: Rumiana.Dimova@mpikg.mpg.de

Abstract

Cells compartmentalize their components in liquid-like condensates[1, 2, 3], which can be reconstituted *in vitro*[4, 5, 6]. Although these condensates interact with membrane-bound organelles[7], the potential of membrane remodeling and the underlying mechanisms are not well understood. Here, we demonstrate that interactions between protein condensates and membranes can lead to remarkable morphological transformations and describe these with theoretical analysis. Modulation of solution salinity or membrane composition drives the condensate-membrane system through two wetting transitions, from dewetting, through a broad regime of partial wetting, to complete wetting. The observed morphologies are governed by the interplay of adhesion, membrane elasticity and interfacial tension. A new phenomenon, namely reticulation or fingering of the condensate-membrane interface is observed when sufficient membrane area is available, producing complex curved structures. Our results highlight the relevance of wetting in cell biology, and pave the way for the design of synthetic membrane-droplet based biomaterials and compartments with tunable properties.

Introduction

The last decade of research has provided ample evidence that in addition to membrane-bound organelles, cells compartmentalize their interior by membraneless-organelles also referred to as macromolecular condensates or coacervates, which behave as liquid droplets. Examples include nucleoli, Cajal bodies, P-bodies, and stress granules, all of which represent liquid protein-rich droplets within the cell[1, 2, 3]. These droplets arise from the condensation of cellular material through liquid-liquid phase separation, and can be reconstituted *in vitro*[4, 5, 6]. This discovery has expanded the search for the different functions of liquid droplets in animal, fungal, and plant systems, that include compartmentalization, sorting of macromolecules, tuning of enzymatic reactions, preservation of cellular fitness, immune response, and temperature sensing[1, 3, 8]. In addition, an aberrant protein condensation has been proposed as an intermediate step in neurodegenerative diseases such as Parkinson and Alzheimer[3, 9]. Thus, the research on

membrane-less organelles has become a very active and strongly interdisciplinary research field[8].

One interesting and hardly explored aspect of liquid droplets is that, although termed "membraneless", they can come into contact and wet membranous compartments[7]. In the last years, it has been found that membrane-droplet interactions are involved in key biological processes like signal transduction in T cells[10], the assembling of virus capsid proteins[11], droplet splitting in the endoplasmic reticulum[12], or the development of tight junctions[13], to name a few. However, a detailed understanding of the underlying physicochemical mechanisms and a systematic characterization of the membrane-droplet interactions is still missing, because these interactions are difficult to assess *in vivo*, to some extent reflecting the small size of the condensates[14]. Here, we develop an *in vitro* system, which allows us to directly probe the condensate-membrane interactions and their mutual remodeling.

So far, membrane-droplet interactions have been studied in the context only of a few *in-vitro* systems. When aqueous two-phase systems (ATPS) consisting of polymer solutions[15, 16, 17, 18, 19] are encapsulated or in contact with giant unilamellar vesicles (GUVs), several biologically relevant processes were demonstrated to occur, namely, outward or inward budding as exo- and endocytic mimetic, formation of membrane nanotubes and fission of vesicle compartments[19]. Another approach consisted of triggering coacervation in the GUV interior by externally changing the pH[20]. Furthermore, membrane tubulation was observed in GUVs decorated with anchored proteins that underwent phase separation[21].

Here, we provide a systematic analysis of the membrane remodeling and wetting behavior of GUVs exposed to water-soluble proteins exhibiting condensation. As a model protein, we employed glycinin, which is one of the most abundant storage proteins in the soybean. Glycinin undergoes self-coacervation in the presence of sodium chloride[6], making it a convenient model system to study the membrane-droplet interaction. When combining glycinin condensates with GUVs we observed condensate-membrane adhesion, partial and complete wetting, condensate-induced budding and a remarkable new feature of this interaction: the complex curving of the membrane-droplet interface producing reticulated membrane structures. The implications of our findings relate not only to droplet-induced morphogenesis of ubiquitous membrane-bound organelles such as the endoplasmic reticulum, but also to the realms of material sciences and synthetic biology in the development of smart soft materials with functions, compartmentation and morphology modulated by wetting.

Results

Membrane wetting by protein condensates

We first evaluated the interaction of glycinin droplets[6] with GUVs made of zwitterionic phosphatidylcholine (see Methods). When the condensates come in contact with the

membranes, they undergo two wetting transitions. At low salt content, the droplets do not interact with the vesicles (dewetted state). Raising the salinity leads to an increased attractive interaction between the droplets and the membrane (partial wetting) until complete wetting, i.e., spreading of the condensates over the whole membrane surface, is reached when the salinity exceeds 180 mM NaCl (Fig. 1a).

The partial wetting morphologies involve three different surface segments, which meet along the contact line (Fig. 1b), as well as three contact angles and surface tensions (Fig. 1c). The contact angles and the mechanical tensions Σ_{ic}^m and Σ_{ie}^m of the two membrane segments depend on the elastic stress within the membrane (Methods, Eqs. 8 and 9) and thus on the size and shape of the vesicle. In contrast, both the interfacial tension Σ_{ce} and the geometric wetting factor Y displayed in Fig. 1d are material parameters, which do not depend on the size and shape of the chosen condensate-vesicle couple. The wetting factor Y is proportional to the adhesion free energy per unit area W of the condensate relative to the exterior solution and can be obtained from the measured contact angles (Methods, Eq. 10).

The experimental data show that glycinin condensates interacting with GUVs exhibit three different wetting regimes separated by two wetting transitions at constant temperature. To the best of our knowledge, this behavior has not been previously reported, even though wetting transitions have been studied for a long time[22, 23, 24]. Remarkably, the system can be easily moved across these wetting transitions by changing the salinity (Fig. 1a) as well as the membrane composition (Fig. 1e,f, Fig. S1).
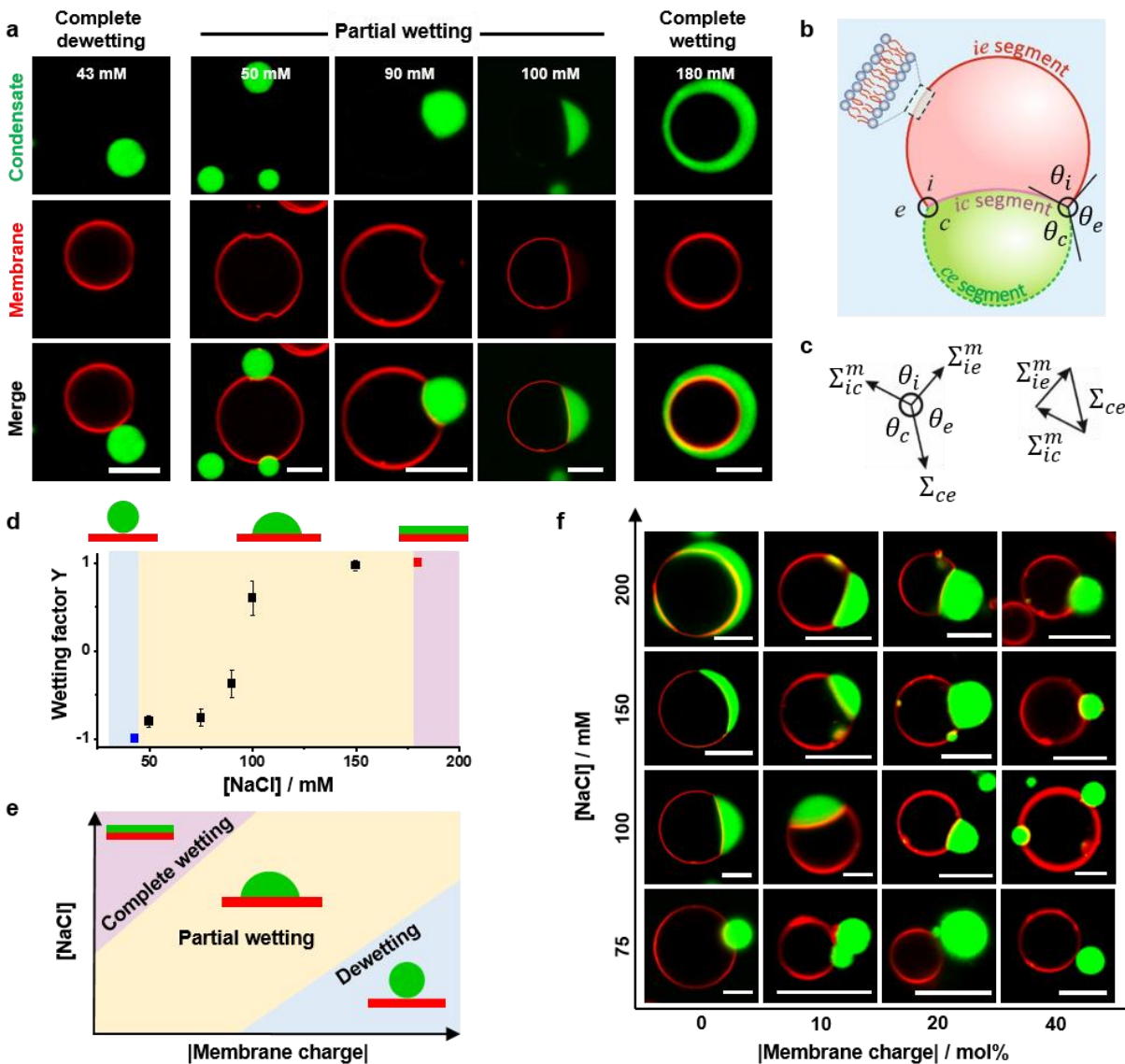
Figure 1: **Distinct wetting morphologies for glycinin condensates (green) in contact with giant vesicles (red)**: **a.** Three wetting regimes separated by two wetting transitions for vesicles made of zwitterionic lipid (DOPC). **b.** Partial wetting is characterized by a contact line. Along this line, the ce interface (dashed green) partitions the membrane into the ie (red) and ic (purple) segments, with the contact angles θ_c, θ_i, and θ_e which sum up to $\theta_c + \theta_i + \theta_e = 360°$. **c.** Force balance between the droplet interfacial tension Σ_{ce} and the mechanical tensions Σ_{ie}^m and Σ_{ic}^m within the two membrane segments. These three tensions form the sides of a triangle (Methods, Eq. 9). **d.** Wetting geometric factor Y (Methods, Eq. 10) as a function of NaCl concentration. The largest possible value $Y = +1$ (red square) corresponds to the transition from partial wetting to complete wetting at [NaCl]≥180 mM, the smallest possible value $Y = -1$ (blue square) to the transition from dewetting to partial wetting at [NaCl]≤43 mM. All data: mean ± SD, n=10 per composition. **e, f.** Combined influence of salinity and membrane surface charge (absolute value; data for 10mol% DOPS and 10mol% DOTAP are combined, see Fig. S1) on wetting morphologies illustrated in a schematic morphology diagram (e) and with representative images (f). All scale bars: 10 μm.

Wetting dynamics and membrane fluidity

In all cases, membrane wetting by the protein condensates was characterized by slow dynamics in the minutes-to-hour range (Fig. 2a, Movie S1). Once touching, the contact angles characterizing the condensate-membrane system required 20-30 min to reach equilibrium (Fig. 2b). This is most likely related to the high viscosity of glycinin condensates ~4.8 kPa s (see Methods). The following results correspond always to the equilibrated final wetting morphology.

Compared to bare (condensate-free) membranes (*ie*, Fig. 1b), vesicle segments in contact with condensates (*ic*) are characterized by lower fluidity as a result of the protein-lipid interaction; the immobile fraction in such membranes is 16±5% measured by FRAP (Fig. 2c,d). This indicates that the condensates not only induce membrane morphological transformations, but also impose dynamic constraints onto the constituting lipid species.
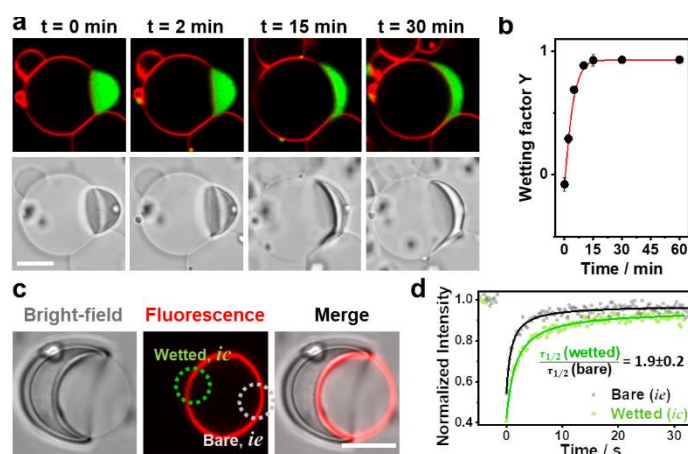

Figure 2: **Wetting and membrane dynamics**: **a.** After the glycinin condensate contacts the membrane (t=0 min), the contact angles change slowly until reaching the final morphology which remains stable for hours; confocal (top) and bright field (bottom) images. **b.** Measured wetting factor for the membrane-condensate system shown in (a); DOPC membrane, 100 mM NaCl. **c.** Fluorescence recovery after photo-bleaching (FRAP) experiments show a decreased fluidity in the membrane part that is wetted by the condensate (*ic* segment in Fig. 1b) compared to the bare (condensate-free, *ie*) one. For these experiments, only the membrane was fluorescently labeled to avoid interferences from the condensate. The dotted circles shown in green/gray indicate the bleached regions for each case (see Fig. S2). **d.** FRAP intensity curves yielding halftimes of recovery $\tau_{1/2}$ (n = 5) from the fitted curves show that condensate wetting slows lipid diffusion by a factor of ~2 (see Methods). Scale bars: 10 μm.

Membrane molding and bridging by condensates

Inspection of the partial wetting morphologies in Fig. 1 and 2 shows that the visible membrane segments *ie* and *ic* are separated by an apparent kink in the membrane shape. The fine structure of this kink corresponds to a highly curved membrane segment, which cannot be resolved in the confocal microscope (but visualized with STED microscopy[25]). It arises from the mechanical balance between the capillary forces,

5

generated by the interfacial tension Σ_{ce} of the condensate-buffer interface, and the membrane bending moment which is proportional to its bending rigidity κ. This mechanical balance implies that the contact line segment acquires a curvature radius of the order of $\sqrt{\kappa/\Sigma_{ce}}$, see Methods. For the typical value $\kappa \simeq 10^{-19}$ J of the bending rigidity and the value $\Sigma_{ce} \simeq 0.5$ mN/m of the interfacial tension (measured here, see Methods), we obtain the curvature radius $\sqrt{\kappa/\Sigma_{ce}} \simeq 140$ nm, which is indeed below the optical resolution limit and appears as a kink in the confocal images.

Membrane wetting by condensates can lead to complex morphologies involving more than one droplet, or more than one GUV (Fig. 3). Complete droplet engulfment can occur, or a condensate can enclose or bridge several GUVs. Thus, the adhesion of the condensates to the membranes can give rise to complex condensate-vesicle architectures of multiple compartments (Fig. 3). The engulfment of the condensates by the vesicle membrane separates the individual droplets from each other and prevents their coalescence. In addition, this process also changes the area of the interface between the condensate and the liquid bulk phase, thereby regulating the diffusive exchange of molecules between the droplets and the bulk phase. Remarkably, hollow condensates, obtained by inducing phase separation within the protein-rich droplets by salinity shift within the coexistence region of the phase diagram (see Methods), can reshape the membranes in a similar way (Fig. 3 g-h), whereby providing additional means of compartmentation.

For condensate-induced budding, the adhesion between condensate and membrane has to overcompensate the bending of the membrane. Both the onset of condensate adhesion and the condensate-induced budding take place when the radius of the condensate droplet exceeds a certain threshold value which is proportional to $\sqrt{\kappa/\Sigma_{ce}}$ and depends on the geometric factor Y in Fig. 1d (Methods, Eqs. 12 and 13). Therefore, the size of the membrane bud, which represents separate membrane compartment, can be controlled by changes in the bending rigidity κ and the interfacial tension Σ_{ce}. For interfacial tension Σ_{ce} around 0.5 mN/m and for bending rigidity $\kappa = 10^{-19}$ J, the minimal radii of droplets and buds become of the order of 15 nm (Methods, Eq. 13). Such nanobuds are no longer resolvable by confocal microscopy but can be studied in molecular dynamics simulations[26].
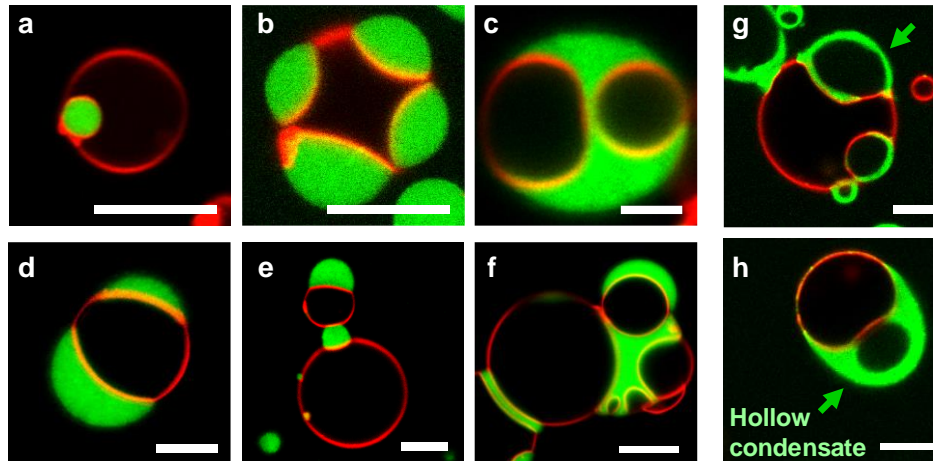
Figure 3: **Membrane molding, vesicle bridging and compartmentation by glycinin condensates**: **a.** Complete engulfment of a droplet by a DOPC GUV at 180 mM NaCl. The engulfment of the condensate is energetically favored by both, the increased contact area with the membrane and the reduced surface area of the ce interface (see Fig. 1b). **b.** Soy-PC GUV at 50mM NaCl in contact with four condensates. Apart from panel c, all membranes exhibit apparent kinks along the contact lines, arising from highly curved contact line segments. **c.** A single condensate engulfing two GUVs by complete wetting at 200 mM NaCl. **d-f**. A single GUV can be wetted by more than one condensate and one condensate can bridge multiple vesicles. **g-h** Hollow condensates (green) in contact with soy-PC GUVs at 50 mM and 150 mM NaCl, respectively (see also Fig. S3) offer additional system compartmentation. Scale bars: 10 µm.

Membrane reticulation induced by protein condensates

Interestingly, vesicles with excess area undergo curving of the membrane/droplet interface (Fig. 4 a,b, Movie S2). We term this process "membrane reticulation" in analogy to the metalwork process of wrinkling the surface of a metal. An even more relevant analogy is provided by the strong resemblance to cells endoplasmic reticulum, despite missing the network-like character (which could be attributed by subsequent fusion of the protrusions as ensured e.g. by fusion proteins) and higher curvature (imposed by adsorbing or scaffolding proteins). The process we observe is also reminiscent of viscous fingering observed when less viscous liquid displaces a more viscous one in porous media[27], although here a membrane separates the fluids, and pressure and porous confinement are absent. Membrane reticulation initiates while the contact angle is stabilizing (see Fig. 4a,b, Movie S2); note that vesicles exhibiting membrane fingering were not taken into account when assessing the wetting factor in Fig. 1, because in such systems the contact angles are ill defined. Once established, the reticular structure remains stable for hours and does not fluctuate (Movie S3). As shown in Fig. 4a (and Movie S2), the contact area between the membrane and the condensate increases by the reticulation. These remarkable structures are only present in vesicles with available excess area and are thus observed more often when the vesicles are osmotically deflated (see Fig. S4). The effect of membrane excess area becomes evident when the membrane

7

tension is increased via micropipette aspiration, which suppresses reticulation leading to smooth vesicle-droplet interfaces (Fig. 4f, Movie S4).

The complex membrane shapes include large protrusions and invaginations in the form of finger-like structures and thin tubes (Fig. 4c-f, Movie S5). It can be seen that the reticulation involves the mutual scaffolding of vesicle and condensates, since both become curved (Fig. 4c,d). Differently from membrane tubulation triggered by spontaneous curvature generation (see e.g.[18, 25]), here protrusions do not have preferred direction and the interface can buckle to either side (see also Fig. S9). Using STED microscopy, we resolved characteristic features and dimensions of the reticulated regions (Figs. 4f, S5).

These intricate and striking morphologies arise from the gain of adhesion energy between droplet and membrane when excess area is pulled out of the ie segment and added to the ic segment. This mechanism implies that the wetting factor Y is positive, and indeed, fingering was observed only for [NaCl] ≥ 100 mM where $Y > 0$. Whether or not reticulation is associated with bending energy penalty depends on the spontaneous curvature of the ic segment. The adhesion of the glycinin-rich droplet implies adsorption of the protein to the membrane, for which one would expect the membrane to bulge towards the droplet as is the case for $Y > 0$. In this case, adhesion and bending act in a synergistic manner. At their surface, condensates exhibit some degree of molecular organization as shown previously by birefringence[6, 28]. We cannot exclude that this surface organization is perturbed by the interaction of the membrane with the proteins at the droplet interface. However, the lipid mobility in the reticulated membrane segment remains similar to that in smooth membrane-condensate segments (compare Figs. S6 and 2c,d). We also confirmed that the membrane integrity is preserved during wetting and reticulation (Fig. S7), and that reticulations are independent of asymmetric buffer conditions (Fig. S8).
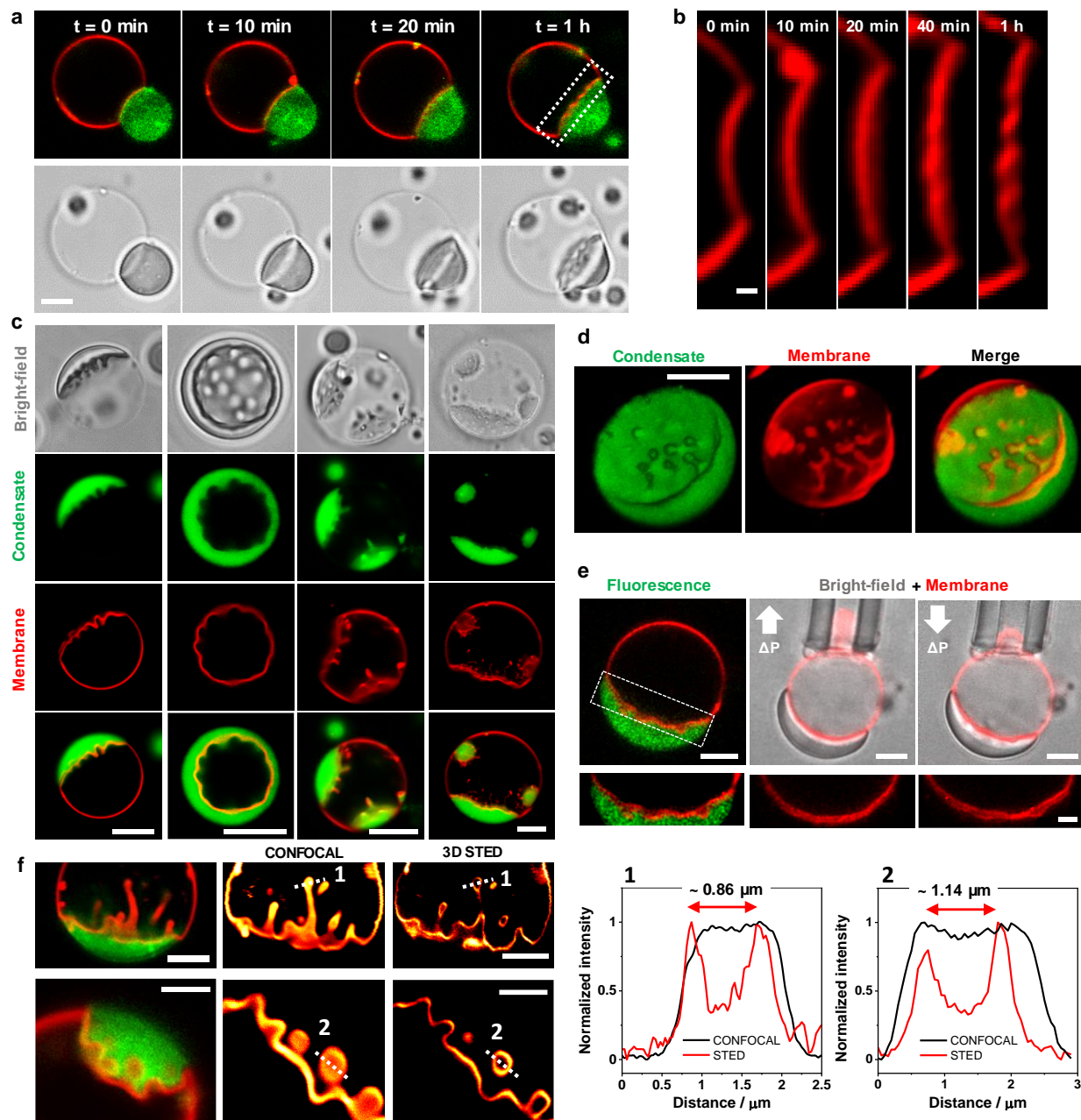
Figure 4: **Membrane reticulation driven by glycinin condensates**: **a.** Mutual membrane-condensate molding and generation of curved structures at the membrane-droplet interface during wetting. **b.** Zoom of the region indicated in (a). **c.** Examples of reticulation morphologies of the condensate-membrane interface. **d.** 3D reconstructions of GUVs in contact with glycinin condensates showing the different reticulation morphologies (see also Fig. S9). **e.** Increasing membrane tension via micropipette aspiration results in the suppression of reticulations and smoothing out of the condensate-membrane interface. The tension threshold needed to suppress the reticulations is (1.0 ± 0.2) mN/m (n=5). When releasing the membrane area by decreasing the tension, reticulations reappeared within a minute (lower panel, up- and down-arrows signify increasing and decreasing suction pressure). A zoom of the membrane region highlighted with white dashed line is shown in the upper panel right. **f.** STED imaging resolves characteristic features of the curved regions. Intensity line profiles along the indicated dashed lines in the micrographs allow for an estimation

of the thickness (left corresponds to the first image and right to the second one). Scale bars in (a, c-f): 5 μm, in (b): 1 μm.

Conclusion

In summary, glycinin condensates interacting with GUVs were observed to undergo two distinct wetting transitions, with a broad intermediate regime of partial wetting (Fig. 1). This behavior should be governed by charge screening, because it can be modulated by changes in the salinity or the membrane charge. In this regime, the interplay between condensate membrane adhesion, capillary forces, and membrane elasticity leads to condensate-induced formation of membrane buds and necks (Fig. 3; Methods, Eq. 13) similarly to deformations observed in storage vacuoles[29]. In addition, when excess membrane area is available, the droplet-membrane interface becomes reticulated generating irregular curved structures (Fig. 4). The complex condensate-membrane morphologies observed here can be tuned by changing the material properties of the condensates and the membrane. In the context of plant cells, glycinin condensation was proposed to occur in the endoplasmic reticulum for the ionic strength range used here[30] and thus, as we demonstrate, can contribute to reshaping it. Our results suggest that protein phase separation and the condensate-mediated membrane structural changes could be a key part in the transport of storage proteins by vesicles during soybean seed formation, as previously hypothesized[30]. Furthermore, these systems could provide templates for the design of multiphase compartments to be used in synthetic biology. Plant proteins like glycinin have the advantage of being widely abundant and economical, which makes them ideal materials for the scale-up processing in biotechnological applications[6]. In this regard, synthetic protocells can now be sequentially assembled, using microfluidics and pico-injection[31], to form droplet-stabilized GUVs and to load them with different biomolecular components[32]. Injecting biomolecular condensates into such GUVs provides a promising method to create protocells that undergo budding and form aqueous sub-compartments in a controlled and reproducible manner, allowing to host chemical or enzymatic reactions[33, 34]. By changing the interfacial tension of the condensates, the size of these compartments can be varied over several orders of magnitude, from tens of nanometers to tens of micrometers. Finally, condensate-membrane interactions triggering reticulation as shown here, demonstrate that they do not only play a role in concentration-regulated phase separation and nucleation[7], but also dramatically mold membranes. Upon encounter with membrane-bound organelles, liquid condensates act as sculptors of intricate membrane structures, generating local curvature, without the involvement of active processes.

Methods

Materials. The phospholipids 1,2-dioleoyl-sn-glycero-3-phosphocholine (DOPC), Soy L-α-phosphatidylcholine (Soy-PC), 1,2-dioleoyl-sn-glycero-3-phospho-L-serine (DOPS), and 1,2-dioleoyl-3-trimethylammonium-propane (DOTAP) and the soluble dye 2-(3-diethylamino-6-diethylazaniumylidene-xanthen-9-yl)-5-sulfo-benzenesulfonate (Sulforhodamine B) were purchased from Avanti Polar Lipids (IL, USA). The fluorescent lipid dye ATTO 647N-DOPE was from ATTO-TEC GmbH (Siegen, Germany). Polyvinyl alcohol (PVA, with MW 145000) was purchased from Merck (Darmstadt, Germany). Chloroform obtained from Merck (Darmstadt, Germany) was of HPLC grade (99.8 %). The lipid stocks were mixed as chloroform solutions at 4 mM, contained 0.5 mol% dye and were stored until use at -20°C. For neutral lipid compositions DOPC was employed, while for the charged membranes were prepared from DOPC:DOPS and DOPC:DOTAP mixtures. Fluorescein isothiocyanate isomer (FITC), sucrose, glucose, dimethyl sulfoxide (DMSO), sodium hydroxide (NaOH) and sodium chloride (NaCl) were obtained from Sigma-Aldrich (Missouri, USA). All solutions were prepared using ultrapure water from SG water purification system (Ultrapure Integra UV plus, SG Wasseraufbereitung) with a resistivity of 18.2 MΩ cm.

Protein purification. Preparation of glycinin was achieved as described in Chen et al.[6]. Briefly, the defatted soy flour was dispersed in 15-fold water in weight and adjusted to pH 7.5 with 2 M NaOH. This slurry was then centrifuged (9000×g, 30 min) at 4°C. Dry sodium bisulfite (SBS) was added to the supernatant (0.98 g SBS/L), the pH of the solution was adjusted to 6.4 with 2 M HCl, and the obtained turbid dispersion was kept at 4 °C overnight. After that, the dispersion was centrifuged (6500×g, 30 min) at 4 °C. The glycinin-rich precipitate was dispersed in 5-fold water and the pH was adjusted to 7. The glycinin solution was then dialyzed against Millipore water for two days at 4 °C and then freeze-dried to acquire the final product with a purity of 97.5%[6].

Protein labeling. A 20 mg/mL soy glycinin solution was prepared in 0.1 M carbonate buffer (pH 9). FITC was dissolved in DMSO at 4 mg/mL. The FITC solution was slowly added into the protein solution with gentle stirring to a final concentration of 0.2 mg/mL. The sample was incubated in the dark while stirring at 23 ºC for 3 h. The excess dye was removed using a PD-10 Sephadex G-25 desalting column (GE Healthcare, IL, USA), and buffer was exchanged for ultrapure water. The pH of the labeled protein solution was adjusted to 7.4 by adding 0.1 M NaOH. For fluorescence microscopy experiments, an aliquot of this solution was added to the working glycinin solution to a final concentration of 4%.

Condensates formation. A glycinin solution at 20 mg/mL was freshly prepared in ultrapure water and pH was adjusted to 7. The solution was filtered to remove any

insoluble materials using 0.45 µm filters and was kept at 4°C before use. To form the condensates, 50 µL of glycinin solution were mixed with the same volume of a NaCl solution of twice the desired final concentration, to obtain a 10 mg/mL solution of glycinin condensates. At this protein concentration, condensates size is optimum for microscopy and distances are big enough so they do not coalesce into a large condensate during the experiment.

Hollow condensates. Salinity shifts in a coacervate suspension towards the phase-coexistence boundary, induced either by decreasing or increasing the salt concentration, results in hollow condensate formation by triggering the formation of protein-poor phase within already formed condensates as previously reported[6]. Here, to generate hollow condensates, first 2 mL of the soy glycinin solution containing 10% (w/w) FITC-labeled protein was mixed with equal volume of 200 mM NaCl solution to induce condensate formation at 100 mM NaCl final concentration. Then, this condensates suspension (100 uL) was mixed with an equal volume of pure water to induced hollow condensates formation at 50 mM NaCl final salinity. To produced hollow condensates at 150 mM, the condensate suspension was mixed with an equal volume of 200 mM NaCl solution and then diluted with 150 mM NaCl solution once more. These steps trigger phase separation within the preformed condensates creating a protein-poor phase within them[6].

Lipid membranes. GUVs were grown using the electroformation method[35]. In brief, 3-4 µL of the lipid stock were spread on two conductive indium tin oxide glasses and kept under vacuum for 1 h. The two glass electrodes were separated by a 2-mm-thick Teflon frame, forming the electroformation chamber. The lipid films were rehydrated with 2 ml of a sucrose solution, matching the osmolarity of the NaCl solution in which the condensates were formed. The osmolarity was adjusted using a freezing point osmometer (Osmomat 3000, Gonotec). An electric AC field (1V, 10 Hz, sinusoidal wave) was applied for one hour at room temperature. Once formed, vesicles were diluted 1:1 in a glucose solution of the same osmolarity, and the suspension of the giant vesicles was stored at room temperature until use. The vesicles were prepared freshly before each experiment.

For the experiments in Fig. S8, the GUVs were prepared with the PVA gel-assisted method[36] which allows vesicle swelling in high salinity conditions. Briefly, two coverslips were cleaned with water and ethanol and dried with nitrogen. PVA solution was prepared by diluting PVA in deionized water to a final concentration of 40mg/mL. A small aliquot (20-50 µL) of the PVA solution was spread on the glass slides and dried for 1 h at 60°C. 3-4 µL of the lipid stock solution were deposited on the PVA-coated glass, and kept for 1 h under vacuum at room temperature. The chamber was assembled with a 2 mm-thick Teflon spacer, and filled with 1 ml of 150 mM NaCl solution. After 30 minutes the vesicles were harvested carefully in order to prevent PVA detaching from the cover glass.

Condensates-membranes suspensions. A 1:10 dilution of the vesicle suspension was made in a solution of the desired final NaCl concentration. The condensate suspension of the same NaCl concentration was diluted 1:4 (with a solution of NaCl at the same concentration) and added to the vesicle suspension at a 15% v/v. After gently mixing the vesicle-condensate suspension, an aliquot was placed on a coverslip (26×56 mm, Waldemar Knittel Glasbearbeitungs GmbH, Germany) for observation with confocal microscopy. The coverslips were previously washed with ethanol and water, and passivated with a 10 mg/mL BSA solution.

For the hollow condensates interaction with vesicles, 20 μL of the hollow condensate suspension was mixed with equal volume of the 10 times diluted soy PC vesicle solution in the same salt concentration.

Confocal microscopy and FRAP. Confocal SP5 or SP8 microscopes equipped with a 63x, 1.2 NA water immersion objective (Leica, Mannheim, Germany) were used for imaging. FITC and ATTO 647N-DOPE were excited using the 488 nm and 633 nm laser lines, respectively.

FRAP measurements were performed on the SP8 setup equipped with a FRAP booster. Circular region of interest (ROI) with diameter of 2 μm on the membrane was bleached during 3 iterative pulses of total time ~3 s. Fluorescence intensities from ROI corresponding to photobleaching were analyzed using ImageJ. Curves were fitted using the formula: $y = (I_0 + I_{max} (x/\tau_{1/2}))/(1 + x/\tau_{1/2})$, where I_{max} is the maximal intensity and $\tau_{1/2}$ is the halftime of recovery.

STED microscopy. An Abberior STED setup (Abberior Instruments GmbH) based on an inverted Olympus IX8 microscope (Olympus Inc., Japan) equipped with a 60x,1.2 NA water immersion objective was used to obtain the super-resolved images. The sample was excited at 640 nm and the depletion laser corresponded to a 775 nm pulsed beam. Alignment was achieved as described previously for our setup[37]. Briefly, 150 nm gold beads (Sigma-Aldrich, USA) were observed in reflection mode to overlap the center of the excitation focus with the center of the depletion focus. Corrections for mismatches between the scattering and fluorescence modes were performed using 100 nm TetraSpeck™ beads (Invitrogen, USA). To measure the resolving power of our setup, crimson beads of 26 nm diameter (FluoSpheres™, Molecular Probe) were used. A measured resolution of ~35 nm was achieved using 80% of the STED laser power (total laser power of 1.25 W), improving by 10-fold the lateral resolution over that of the corresponding excitation laser[37]. For our experiments, 3D STED was more suitable than 2D STED, since we could eliminate the interference of out-of-focus signal coming from the curved regions of the membrane (see Fig. S5). For the images shown in Fig. 4f and S5, the pixel size is 50 nm and the pixel dwell time is 10 μs.

13

Micropipette aspiration. Micropipettes were formed by pulling glass capillaries (World Precision Instruments Inc.) with a pipette puller (Sutter Instruments, Novato, CA). Pipette tips were cut using a microforge (Narishige, Tokyo, Japan) to obtain smooth tips with inner diameter between 6-10 μm. The pipette tips were coated with 2 mg/mL solution of casein (Sigma) to prevent adhesion. Latex microspheres of 6 μm diameter (Polysciences Inc., PA, USA) were used to determine the zero-pressure level. The aspiration pressure was controlled through adjustments in the height of a connected water reservoir mounted on a linear translational stage (M-531.PD; Physik Instrumente, Germany). Images were analyzed using the ImageJ software.

Wetting geometries and contact angles. All wetting geometries involve three aqueous solutions: the interior solution i within the vesicle, the exterior buffer e, and the glycinin condensate c. These aqueous solutions are separated by three surface segments (Fig. 1b). The glycinin condensate c is separated from the exterior buffer e by the ce interface. When the interface forms a contact line with the membrane, this line partitions the membrane into two membrane segments. The membrane segment ic forms the contact area with the condensate whereas the other membrane segment ie is exposed to the exterior buffer. At the contact line, the three surface segments form three apparent contact angles θ_c, θ_i, and θ_e that add up to 360° (Fig. 1b). For partial wetting, all three contact angles have values between 0° and 180°. Dewetting of the condensate corresponds to the limiting case with contact angle θ_c = 180° whereas complete wetting by the condensate is characterized by θ_c = 0.

Contact angle determination. In order to adequately extract information on the contact angles between the different interfaces from microscopy projections, it is necessary that in the projected image, the rotational axis of symmetry of the vesicle-droplet system lies in the image plane (see Fig. S10). Otherwise, a wrong projection will lead to misleading values of the system geometry and the contact angles. Once the 3D image of the vesicle and the droplet is acquired (and reoriented to obtain correct projection), we consider the three spherical caps of the vesicle, the droplet and the vesicle-droplet interface, and fit circles to the contours to extract the different radii and centers positions as defined in Fig. S2. In this manner, all the apparent angles can be defined by the following expressions[38]:

$$sin\theta_i \quad = \frac{R_4}{R_1 R_3}\left(\sqrt{R_1^2 - R_4^2} + \sqrt{R_3^2 - R_4^2}\right) \tag{1}$$

$$sin\theta_c \quad = \frac{R_4}{R_3 R_2}\left(\sqrt{R_3^2 - R_4^2} - \sqrt{R_2^2 - R_4^2}\right) \tag{2}$$

With $R_1 \geq R_2$

14

$$sin\theta_e = \frac{R_4}{R_1 R_2}\left(\sqrt{R_1^2 - R_4^2} + \sqrt{R_2^2 - R_4^2}\right) \tag{3}$$

For the case of the C_3 being located above C_1 (when the membrane is curved towards the droplet), these relations become[38]:

$$sin\theta_i = \frac{R_4}{R_1 R_3}\left(\sqrt{R_1^2 - R_4^2} - \sqrt{R_3^2 - R_4^2}\right) \tag{4}$$

$$sin\theta_c = \frac{R_4}{R_3 R_2}\left(\sqrt{R_3^2 - R_4^2} + \sqrt{R_2^2 - R_4^2}\right) \tag{5}$$

With $R_1 \geq R_3$

$$sin\theta_e = \frac{R_4}{R_1 R_2}\left(\sqrt{R_1^2 - R_4^2} + \sqrt{R_2^2 - R_4^2}\right) \tag{6}$$

where R_1, R_2, and R_3 are the radius of the circles fitting the vesicle, the droplet and the contact line, respectively. R_4 is the apparent contact line radius, that can be obtained as follows:

$$R_4 = \frac{2}{d_{12}}\sqrt{s(s - d_{12})(s - R_2)(s - R_1)} \tag{7}$$

where $s = \frac{R_1 + R_2 + d_{12}}{2}$. In this manner, the only input parameters required to be measured from the projection images are the radii of the fitted circles (R_1, R_2, and R_3) and the distance between the centers of the vesicle and the droplet circles (d_{12}).

Note that the above analysis is only valid for spherical caps morphologies as shown in Fig. 1-2, and cannot be applied to reticulated membrane-droplet interfaces (Fig 4), which do not fulfill the spherical cap condition.

From contact angles to fluid-elastic parameters. The contact angles in Fig. 1, are related to the different surface tensions that pull the three surface segments along the contact line, see Fig. 1b,c. One of these surface tensions is provided by the interfacial tension Σ_{ce} of the condensate-buffer interface. The latter tension is balanced by the difference Σ_{ie}- Σ_{ic} between the membrane tensions Σ_{ie}^m and Σ_{ic}^m of the two membrane segments. This balance implies that the three surface tensions form the sides of a triangle (Fig. 1c). In general, membrane tensions can be decomposed into different contributions[38]. The mechanical tensions of the two membrane segments are given by

$$\Sigma_{ie}^m = \Sigma \quad \text{and} \quad \Sigma_{ic}^m = \Sigma + W, \tag{8}$$

where Σ denotes the elastic stress within the membrane and W represents the affinity contrast between the exterior buffer and the condensate phase, i.e., the adhesion free

15

energy per unit area of the condensate phase relative to the external buffer[38]. Thus, the affinity contrast W is negative and positive if the membrane prefers the condensate over the buffer and vice versa.

The elastic stress Σ can be theoretically described in two apparently distinct but nevertheless equivalent ways[39]. First, it can be expressed in the intuitive form $\Sigma = K_A(A - A_0)/A_0$ with the area compressibility modulus K_A and the area dilation $(A - A_0)/A_0$, where A is the total membrane area and A_0 denotes the area of the tensionless membrane in the absence of the condensate droplet. Lipid bilayers have a typical area compressibility modulus of the order of 10^2 mN/m [40] and rupture for relatively small area dilations of a few percent. Therefore, the tension of rupture is of the order of a few mN/m. Second, the elastic stress Σ can also be used as a Lagrange multiplier to minimize the free energy of the condensate-membrane system under the constraint that the total membrane area has the prescribed value A. As a consequence, the elastic stress Σ as well as the membrane tensions Σ_{ie}^m and Σ_{ic}^m in Eq. 8 depend on the size and shape of the membrane segments, in strong contrast to the interfacial tension Σ_{ce} which represents a material parameter that is independent of the size and shape of the liquid-liquid interface.

Furthermore, the tension triangle in Fig. 1c implies the relationships

$$\frac{\Sigma_{ie}^m}{\Sigma_{ce}} = \frac{\Sigma}{\Sigma_{ce}} = \frac{\sin\theta_c}{\sin\theta_i} \quad \text{and} \quad \frac{\Sigma_{ic}^m}{\Sigma_{ce}} = \frac{\Sigma + W}{\Sigma_{ce}} = \frac{\sin\theta_e}{\sin\theta_i} \tag{9}$$

between the surface tensions and the contact angles. When we consider the difference $\Sigma_{ie}^m - \Sigma_{ic}^m$, the geometry-dependent elastic stress Σ drops out and we obtain $\Sigma_{ie}^m - \Sigma_{ic}^m = -W = Y\Sigma_{ce}$ where the dimensionless wetting factor

$$Y \equiv \frac{\sin\theta_c - \sin\theta_e}{\sin\theta_i} \quad \text{satisfies} \quad -1 \leq Y \leq 1 \tag{10}$$

As plotted in Fig. 1d the latter factor increases with increasing salinity. The factor Y is completely determined by the three contact angles and can, thus, be obtained from the optical images (Fig. 1d). The smallest possible value $Y = -1$ corresponds to the transition from partial wetting to dewetting; the largest possible value $Y = +1$ to the transition from partial to complete wetting. The dimensionless factor Y is positive if the membrane prefers the condensate over the exterior buffer and negative otherwise. It then follows from the data in Fig. 1d that the membrane prefers the condensate for molar salt concentrations $X > X_0 \simeq 93$ mM and the exterior buffer for $X < X_0$. For $X = X_0$, the geometric factor Y vanishes, corresponding to equal contact angles $\theta_c = \theta_e$ and no affinity contrast between the condensate and the exterior buffer. Therefore, by measuring the geometric factor Y as a function of the salinity or another control parameter, we obtain the affinity contrast $W = \Sigma_{ie}^m - \Sigma_{ic}^m = -Y\Sigma_{ce}$ in units of the interfacial tension Σ_{ce} as a function of this control parameter.

Fine structure of the contact line. In the optical images, the membrane shape has an apparent kink along the contact line, which corresponds to a highly curved membrane segment. This contact line segment is located between the visible segments ie and ic (Figs. 1,2). The corresponding principal curvature radius $R_\perp$ perpendicular to the contact line can be estimated as follows. We smoothen the sharp kink of the membrane shape at the apparent contact line by a toroidal membrane segment that joins the ie and ic segments with a common tangent. The curvature $1/R_\perp$ of this segment is much larger than (i) the mean curvatures of the two visible membrane segments, (ii) the mean curvature of the condensate-buffer interface, and (iii) the inverse radius of the contact line, which represents the second principal curvature of the contact line segment. Thus, on the scale of the curvature radius $R_\perp$, the two visible membrane segments and the condensate-buffer interface are essentially planar. We are then led to consider a wedge geometry in which the ie and ic membrane segments form the planar faces of the wedge and the contact line segment becomes a cylindrical segment with curvature radius $R_\perp$ that joins the faces of the wedge with a common tangent. The angle of the wedge is equal to the contact angle θ_i, opening towards the interior aqueous solution. The intersection of the condensate-buffer interface with the cylindrical contact line segment is determined by the curvature radius $R_\perp$ as well as by the contact angles. We then vary $R_\perp$ to minimize the sum of the bending energy of the membrane and the interfacial free energy of the condensate-buffer interface for fixed values of the contact angles. The bending energy is proportional to the bending rigidity κ and the interfacial free energy to the interfacial tension Σ_{ce}. As a result, we find that the curvature radius $R_\perp$ is proportional to $\sqrt{\kappa/\Sigma_{ce}}$ with a prefactor that depends on the contact angles. Furthermore, when the contact line has the length L_{co}, its excess free energy has the form $L_{co}\lambda_{eff}$ which defines the effective line tension λ_{eff}. This line tension is proportional to $\sqrt{\kappa/\Sigma_{ce}}$ with an angle-dependent prefactor.

Condition for the onset of condensate adhesion. Consider a spherical condensate droplet of radius R adjacent to a weakly curved GUV membrane. When the membrane starts to spread over the droplet, it acquires a small contact area ΔA_{ic}. The corresponding change in free energy has the form

$$\Delta E = \Delta A_{ic}\left[-(1+Y)\Sigma_{ce} + 2\frac{\kappa}{R^2}\right] + L_{co}\lambda_{eff} \tag{11}$$

The first term describes the reduction in the free energy by the adhesion of condensate and membrane, the second term the increase in the bending energy of the membrane, and the third term represents the line energy of the contact line with length L_{co} and effective line tension λ_{eff}. In the second term of Eq. 11, we ignored a possible change in the curvature radius of the ic segment. Adhesion of the condensate droplet is energetically favorable if $\Delta E < 0$ which leads, for $\lambda_{eff} > 0$, to the necessary condition

$$-(1+Y)\Sigma_{ce} + 2\frac{\kappa}{R^2} < 0 \tag{12}$$

for the adhesion of the condensate droplet to the membrane. This inequality implies that the droplet radius R must exceed a certain threshold value in order for the droplet to adhere to the membrane. For 50 and 75 mM NaCl as in Fig. 1d, the glycinin droplets partially wet the membrane with a large contact angle θ_c, corresponding to $Y = -0.8$ and $Y = -0.76$ and a minimal droplet radius of 850 nm, in agreement with our observations.

Complete engulfment of condensate droplets. A spherical condensate droplet with radius R, which does not adhere to the GUV membrane, has the interfacial free energy $4\pi R^2 \Sigma_{ce}$. When this droplet is completely engulfed by the membrane, the membrane forms a spherical ic membrane segment of radius R with bending energy $8\pi\kappa$ and adhesion free energy $4\pi R^2 W = -4\pi R^2 Y \Sigma_{ce}$ with the geometric factor Y as in Fig. 1d. The condensate droplet prefers complete engulfment over its non-adhering state if $4\pi R^2 \Sigma_{ce} > 8\pi\kappa - 4\pi R^2 Y \Sigma_{ce}$ or

$$R > \sqrt{\frac{2}{1+Y}}\sqrt{\frac{\kappa}{\Sigma_{ce}}} \tag{13}$$

which is identical with the condition in Eq. 11. Here, we have implicitly assumed that the membrane is coupled to an area reservoir and is thus characterized by a low elastic stress Σ. When the membrane completely engulfs the condensate droplet, it forms a bud which is connected to the mother membrane by a closed membrane neck[38].

This budding process can be used to generate membrane compartments of various sizes. Because the minimal droplet radius for complete engulfment is proportional to $\sqrt{\kappa/\Sigma_{ce}}$, the size is controlled by the magnitude of the bending rigidity and the interfacial tension Σ_{ce}. For interfacial tension $\Sigma_{ce} = 0.5$ mN/m (as measured here for glycinin) and bending rigidity $k = 10^{-19}$ J, the minimal droplet radius for complete engulfment becomes of the order of 15 nm, which is no longer detectable by confocal microscopy but can be observed in molecular dynamics simulations[26]. When a condensate droplet adheres to a membrane, it is bounded by two surfaces, provided by the interface with the coexisting liquid phase and the adhesion zone with the membrane. Fast diffusive exchange of molecules between the condensate and the other liquid phase is only possible across the interface between these two phases but not across the condensate-membrane adhesion zone. During bud formation, the area of the liquid-liquid interface is strongly reduced (Fig. 3). Therefore, the engulfment process could be used as an efficient regulation mechanism for the exchange of molecules across the liquid-liquid interface.

Glycinin condensates material properties.

Measuring the material properties of biomolecular condensates is a challenging task, that typically relies on fluorescence recovery after photobleaching (FRAP) measurements and on quantifying the coalescence kinetics of two condensate droplets[2, 41, 42]. These techniques can provide information about the viscosity[41, 42] and can yield the inverse

capillarity number (i.e. the ratio of surface tension/viscosity)[2], respectively. Recently, the micropipette aspiration method has been applied to quantify both, the viscosity and the surface tension of condensate droplets, provided that they behave as Newtonian fluids at the experimental time scale (>1s)[43].

In a previous study, glycinin condensates were shown to exhibit only negligible fluorescence recovery in FRAP experiments, suggesting a highly viscous environment[6]. By using the condensate coalescence assay, the inverse capillary number of glycinin droplets was measured to be $\eta/\Sigma_{ce} \approx$ 9.69 s/µm[6]. A very rough estimate of the surface tension based on the molecular size of glycinin yielded the value of $\Sigma_{ce} \approx$ 0.16 mN/m, implying for the viscosity $\eta \approx$1.6 kPa.s [6].

Here, we attempted to measure directly the viscosity and surface tension by means of the micropipette aspiration method. However, as can be observed in Fig. S11, glycinin condensates do not flow inside the pipette. The aspiration can only proceed until a pressure value (the maximum suction pressure achieved by our setup is up to 2500 Nm⁻²) beyond which the pipette gets clogged and the condensate cannot be further aspirated nor released. This outcome does not depend on the condensate/pipette diameter ratio. In addition, aging effects were discarded since they occur at time scales (days) [6, 44] longer than those required for our experiments (minutes-hours). Pipette clogging prevented us from measuring the viscosity, but we could estimate the tension by means of the Laplace equation $\Sigma_{ce} = \Delta P\, R_{cap}/2(1 - \frac{R_{cap}}{R_{drop}})$, where ΔP is the applied pressure, and R_{cap} and R_{drop} are respectively the radius of the spherical cap formed by the part of the droplet inside the pipette and the radius of the droplet outside the pipette (see sketch in Fig. S11b). The tension value obtained in this way for glycinin droplets in the presence of 100 mM NaCl is Σ_{ce}= (0.5 ± 0.3) mN/m (n=5), which is of the same order of magnitude of the value previously estimated from the coalescence assay. The condensate viscosity we obtain is $\eta \approx$4.8 kPa.s. The glycinin surface tension value is similar to that of LAF-1[45] and PolyR[46] condensates, and the viscosity, close to that of the nucleus[47], as is summarized in Fig 1 of the work of Wang et al.[43] This particular combination of high surface tension and high viscosity might be related to the structural characteristics of these condensates. Whilst more coacervation-prone proteins feature mostly one type of polypeptide[48, 49], glycinin is a hexamer[50, 51] implying that it is characterized by a more bulky and complex structure. This could explain the reduced diffusion and high viscosity of the condensates.

Supplementary Information Figs. S1-S11 and Videos 1-5.

References

1.   Banani SF, Lee HO, Hyman AA, Rosen MK. Biomolecular condensates: organizers of cellular biochemistry. *Nat Rev Mol Cell Biol* 2017, **18**(5)**:** 285-298.

2.   Brangwynne CP, Eckmann CR, Courson DS, Rybarska A, Hoege C, Gharakhani J*, et al.* Germline P Granules Are Liquid Droplets That Localize by Controlled Dissolution/Condensation. *Science* 2009, **324**(5935)**:** 1729-1732.

3.   Alberti S, Hyman AA. Biomolecular condensates at the nexus of cellular stress, protein aggregation disease and ageing. *Nature Reviews Molecular Cell Biology* 2021, **22**(3)**:** 196-213.

4.   Li P, Banjade S, Cheng H-C, Kim S, Chen B, Guo L*, et al.* Phase transitions in the assembly of multivalent signalling proteins. *Nature* 2012, **483**(7389)**:** 336-340.

5.   Patel A, Lee Hyun O, Jawerth L, Maharana S, Jahnel M, Hein Marco Y*, et al.* A Liquid-to-Solid Phase Transition of the ALS Protein FUS Accelerated by Disease Mutation. *Cell* 2015, **162**(5)**:** 1066-1077.

6.   Chen N, Zhao Z, Wang Y, Dimova R. Resolving the Mechanisms of Soy Glycinin Self-Coacervation and Hollow-Condensate Formation. *ACS Macro Letters* 2020, **9**(12)**:** 1844-1852.

7.   Snead WT, Gladfelter AS. The Control Centers of Biomolecular Phase Separation: How Membrane Surfaces, PTMs, and Active Processes Regulate Condensation. *Molecular Cell* 2019, **76**(2)**:** 295-305.

8.   Emenecker RJ, Holehouse AS, Strader LC. Biological Phase Separation and Biomolecular Condensates in Plants. *Annual Review of Plant Biology* 2021, **72**(1)**:** 17-46.

20

9. Wegmann S, Eftekharzadeh B, Tepper K, Zoltowska KM, Bennett RE, Dujardin S*, et al.* Tau protein liquid–liquid phase separation can initiate tau aggregation. *The EMBO Journal* 2018, **37**(7)**:** e98049.

10. Su X, Ditlev JA, Hui E, Xing W, Banjade S, Okrut J*, et al.* Phase separation of signaling molecules promotes T cell receptor signal transduction. *Science* 2016, **352**(6285)**:** 595-599.

11. Ambroggio EE, Costa Navarro GS, Pérez Socas LB, Bagatolli LA, Gamarnik AV. Dengue and Zika virus capsid proteins bind to membranes and self-assemble into liquid droplets with nucleic acids. *Journal of Biological Chemistry* 2021, **297**(3)**:** 101059.

12. Lee JE, Cathey PI, Wu H, Parker R, Voeltz GK. Endoplasmic reticulum contact sites regulate the dynamics of membraneless organelles. *Science* 2020, **367**(6477)**:** eaay7108.

13. Beutel O, Maraspini R, Pombo-García K, Martin-Lemaitre C, Honigmann A. Phase Separation of Zonula Occludens Proteins Drives Formation of Tight Junctions. *Cell* 2019, **179**(4)**:** 923-936.e911.

14. Bergeron-Sandoval L-P, Kumar S, Heris Hossein K, Chang Catherine LA, Cornell Caitlin E, Keller Sarah L*, et al.* Endocytic proteins with prion-like domains form viscoelastic condensates that enable membrane remodeling. *Proceedings of the National Academy of Sciences* 2021, **118**(50)**:** e2113789118.

15. Helfrich MR, Mangeney-Slavin LK, Long MS, Djoko Y, Keating CD. Aqueous phase separation in giant vesicles. *Journal of the American Chemical Society* 2002, **124**(45)**:** 13374-13375.

16. Li Y, Lipowsky R, Dimova R. Transition from complete to partial wetting within membrane compartments. *Journal of the American Chemical Society* 2008, **130**(37)**:** 12252-12253.

17. Keating CD. Aqueous Phase Separation as a Possible Route to Compartmentalization of Biological Molecules. *Acc Chem Res* 2012, **45**(12)**:** 2114-2124.

18.   Liu Y, Lipowsky R, Dimova R. Giant Vesicles Encapsulating Aqueous Two-Phase Systems: From Phase Diagrams to Membrane Shape Transformations. *Frontiers in Chemistry* 2019, **7:** 213.

19.   Dimova R, Lipowsky R. Giant Vesicles Exposed to Aqueous Two-Phase Systems: Membrane Wetting, Budding Processes, and Spontaneous Tubulation. *Advanced Materials Interfaces* 2017, **4**(1)**:** 1600451.

20.   Last MGF, Deshpande S, Dekker C. pH-Controlled Coacervate–Membrane Interactions within Liposomes. *ACS Nano* 2020, **14**(4)**:** 4487-4498.

21.   Yuan F, Alimohamadi H, Bakka B, Trementozzi AN, Day KJ, Fawzi NL*, et al.* Membrane bending by protein phase separation. *Proceedings of the National Academy of Sciences* 2021, **118**(11)**:** e2017435118.

22.   Cahn JW. Critical point wetting. *The Journal of Chemical Physics* 1977, **66**(8)**:** 3667-3672.

23.   Gau H, Herminghaus S, Lenz P, Lipowsky R. Liquid Morphologies on Structured Surfaces: From Microchannels to Microchips. *Science* 1999, **283**(5398)**:** 46-49.

24.   Bonn D, Eggers J, Indekeu J, Meunier J, Rolley E. Wetting and spreading. *Reviews of Modern Physics* 2009, **81**(2)**:** 739-805.

25.   Zhao Z, Roy D, Steinkühler J, Robinson T, Lipowsky R, Dimova R. Super-resolution imaging of highly curved membrane structures in giant vesicles encapsulating molecular condensates. *Advanced Materials* 2021, **34**(4)**:** 2106633.

26.   Satarifard V, Grafmüller A, Lipowsky R. Nanodroplets at Membranes Create Tight-Lipped Membrane Necks via Negative Line Tension. *ACS Nano* 2018, **12**(12)**:** 12424-12435.

27.   Homsy GM. Viscous fingering in porous media. *Annual review of fluid mechanics* 1987, **19**(1)**:** 271-311.

28.   Alshareedah I, Moosa MM, Raju M, Potoyan DA, Banerjee PR. Phase transition of RNA–protein complexes into ordered hollow condensates. *Proceedings of the National Academy of Sciences* 2020**:** 201922365.

29.   Feeney M, Kittelmann M, Menassa R, Hawes C, Frigerio L. Protein Storage Vacuoles Originate from Remodeled Preexisting Vacuoles in Arabidopsis thaliana *Plant Physiology* 2018, **177**(1)**:** 241-254.

30.   Mori T, Maruyama N, Nishizawa K, Higasa T, Yagasaki K, Ishimoto M*, et al.* The composition of newly synthesized proteins in the endoplasmic reticulum determines the transport pathways of soybean seed storage proteins. *The Plant Journal* 2004, **40**(2)**:** 238-249.

31.   Abate AR, Hung T, Mary P, Agresti JJ, Weitz DA. High-throughput injection with microfluidics using picoinjectors. *Proceedings of the National Academy of Sciences* 2010, **107**(45)**:** 19163-19166.

32.   Weiss M, Frohnmayer JP, Benk LT, Haller B, Janiesch J-W, Heitkamp T*, et al.* Sequential bottom-up assembly of mechanically stabilized synthetic cells by microfluidics. *Nat Mater* 2018, **17:** 89-96.

33.   Deshpande S, Brandenburg F, Lau A, Last MGF, Spoelstra WK, Reese L*, et al.* Spatiotemporal control of coacervate formation within liposomes. *Nature Communications* 2019, **10**(1)**:** 1800.

34.   Love C, Steinkühler J, Gonzales DT, Yandrapalli N, Robinson T, Dimova R*, et al.* Reversible pH-Responsive Coacervate Formation in Lipid Vesicles Activates Dormant Enzymatic Reactions. *Angew Chem Int Ed* 2020, **59**(15)**:** 5950-5957.

35.   Angelova MI, Dimitrov DS. Liposome Electroformation. *Faraday Discussions* 1986, **81:** 303-311.

36.   Weinberger A, Tsai FC, Koenderink GH, Schmidt TF, Itri R, Meier W*, et al.* Gel-Assisted Formation of Giant Unilamellar Vesicles. *Biophys J* 2013, **105**(1)**:** 154-164.

37.   Zhao Z, Roy D, Steinkühler J, Robinson T, Lipowsky R, Dimova R. Super-Resolution Imaging of Highly Curved Membrane Structures in Giant Vesicles Encapsulating Molecular Condensates. *Adv Mater* 2022, **34**(4)**:** 2106633.

38.   Lipowsky R. Response of Membranes and Vesicles to Capillary Forces Arising from Aqueous Two-Phase Systems and Water-in-Water Droplets. *The Journal of Physical Chemistry B* 2018, **122**(13)**:** 3572-3586.

39.   Lipowsky R. Coupling of bending and stretching deformations in vesicle membranes. *Adv Colloid Interface Sci* 2014, **208:** 14-24.

40.   Rawicz W, Olbrich KC, McIntosh T, Needham D, Evans E. Effect of chain length and unsaturation on elasticity of lipid bilayers. *Biophys J* 2000, **79**(1)**:** 328-339.

41.   Schuster BS, Regy RM, Dolan EM, Kanchi Ranganath A, Jovic N, Khare SD*, et al.* Biomolecular Condensates: Sequence Determinants of Phase Separation, Microstructural Organization, Enzymatic Activity, and Material Properties. *The Journal of Physical Chemistry B* 2021, **125**(14)**:** 3441-3451.

42.   Taylor NO, Wei M-T, Stone HA, Brangwynne CP. Quantifying Dynamics in Phase-Separated Condensates Using Fluorescence Recovery after Photobleaching. *Biophysical Journal* 2019, **117**(7)**:** 1285-1300.

43.   Wang H, Kelley FM, Milovanovic D, Schuster BS, Shi Z. Surface tension and viscosity of protein condensates quantified by micropipette aspiration. *Biophysical Reports* 2021, **1**(1)**:** 100011.

44.   Jawerth L, Fischer-Friedrich E, Saha S, Wang J, Franzmann T, Zhang X*, et al.* Protein condensates as aging Maxwell fluids. *Science* 2020, **370**(6522)**:** 1317-1323.

45.   Elbaum-Garfinkle S, Kim Y, Szczepaniak K, Chen Carlos C-H, Eckmann Christian R, Myong S*, et al.* The disordered P granule protein LAF-1 drives phase separation into droplets with tunable viscosity and dynamics. *Proceedings of the National Academy of Sciences* 2015, **112**(23)**:** 7189-7194.

46.   Fisher RS, Elbaum-Garfinkle S. Tunable multiphase dynamics of arginine and lysine liquid condensates. *Nature Communications* 2020, **11**(1)**:** 4628.

47. Caragine CM, Haley SC, Zidovska A. Surface Fluctuations and Coalescence of Nucleolar Droplets in the Human Cell Nucleus. *Physical Review Letters* 2018, **121**(14)**:** 148101.

48. Wei W, Tan Y, Martinez Rodriguez NR, Yu J, Israelachvili JN, Waite JH. A mussel-derived one component adhesive coacervate. *Acta Biomaterialia* 2014, **10**(4)**:** 1663-1670.

49. Gabryelczyk B, Cai H, Shi X, Sun Y, Swinkels PJM, Salentinig S*, et al.* Hydrogen bond guidance and aromatic stacking drive liquid-liquid phase separation of intrinsically disordered histidine-rich peptides. *Nature Communications* 2019, **10**(1)**:** 5465.

50. Adachi M, Kanamori J, Masuda T, Yagasaki K, Kitamura K, Mikami B*, et al.* Crystal structure of soybean 11S globulin: Glycinin A3B4 homohexamer. *Proceedings of the National Academy of Sciences* 2003, **100**(12)**:** 7395-7400.

51. Adachi M, Takenaka Y, Gidamis AB, Mikami B, Utsumi S. Crystal Structure of Soybean Proglycinin A1aB1b Homotrimer. *Journal of Molecular Biology* 2001, **305**(2)**:** 291-305.